

Article

# Strain Induced Metal–Insulator Transition of Magnetic SrRuO<sub>3</sub> Single Layer in SrRuO<sub>3</sub>/SrTiO<sub>3</sub> Superlattice

Angus Huang <sup>1,†</sup>, Sheng-Hsiung Hung <sup>1,†</sup> and Horng-Tay Jeng <sup>1,2,3,\*</sup>

<sup>1</sup> Department of Physics, National Tsing Hua University, Hsinchu 30013, Taiwan; rabbit4a9@gmail.com (A.H.); feynman0121@gmail.com (S.-H.H.)

<sup>2</sup> Physics Division, National Center for Theoretical Sciences, Hsinchu 30013, Taiwan

<sup>3</sup> Institute of Physics, Academia Sinica, Taipei 11529, Taiwan

\* Correspondence: jeng@phys.nthu.edu.tw

† These authors contributed equally to this work.

Received: 21 September 2018; Accepted: 31 October 2018; Published: 3 November 2018



**Abstract:** Ferromagnetic phase in a two-dimensional system plays an important role not only in applications but also in studies of phase transition theory. Among numerous ferromagnetic materials, SrRuO<sub>3</sub> is famous for its half-metallicity, itinerant ferromagnetism and non-Fermi liquid metallicity. Single layer SrRuO<sub>3</sub> in SrRuO<sub>3</sub>/SrTiO<sub>3</sub> (SRO/STO) superlattice has been predicted as a two-dimensional half-metallic ferromagnetic system based on density functional theory (DFT). However, experiments show that metal–insulator transition associated with ferro–antiferromagnetism (FM–AFM) transition occurs when the thickness of SRO is less than 4 u.c. Combining DFT calculations with Monte Carlo simulations, we demonstrate in this work that the bulk ferromagnetic metallicity can be realized in single layer SRO in SRO/STO superlattice by manipulating the strain effect to trigger the metal–insulator transition, achieving two-dimensional (2D) half-metallic SRO thin film beyond the experimental observation of AFM insulator. Our results pave a new route to fulfill the ultrathin spin-polarized-2D electron gas (SP-2DEG).

**Keywords:** metal–insulator transition; superlattice; half-metal; magnetism; 2DEG

## 1. Introduction

Magnetic thin films and two-dimensional magnetic materials have attracted worldwide attention owing to the interesting physical phenomenon and various applications. For example, the spin current transport in a confined thin film implies the prospect to control the spin signal in the nano-scale. Several spintronic devices have been proposed or implemented, such as the magnetic tunnel junction [1–3], magnetic random access memory (MRAM) [4–6], and solid-state drive (SSD). To improve the efficiency of spin devices, magnetic materials or magnetic heterostructures, particularly magnetic thin films composed of transition metal oxide (TMO), have been proposed and caught many researcher’s eyes. Thanks to the huge family of TMO, many heterostructures, such as LaAlO<sub>3</sub>/SrTiO<sub>3</sub> [7,8], BaTiO<sub>3</sub>/La<sub>1–x</sub>Sr<sub>x</sub>MnO<sub>3</sub> [9–11], BiFeO<sub>3</sub>/La<sub>1–x</sub>Sr<sub>x</sub>MnO<sub>3</sub> [12] and so on, provide diverse, unusual properties for different kinds of applications.

The 4d ferromagnetic metal SrRuO<sub>3</sub> (SRO) with Currie temperature  $T_C \simeq 150$  K [13] has been studied in many heterostructures [14–16]. Unusual properties such as the half-metallicity [17–20], itinerant ferromagnetism [21,22] and non-Fermi liquid [23,24] in SRO have been well documented. In particular, monolayer SRO sandwiched by SrTiO<sub>3</sub> (STO) is predicted as a two-dimensional half-metallic electron gas based on DFT calculations [25]. However, experiments show that the SRO thin film exhibits a metal–insulator transition below 4 unit cell (u.c.) [26,27]. Several theoretical studies have tried to

explain this metal–insulator transition. However, most of them provide only partially correct properties for SRO thin films, such as correct insulating behaviors for two and three layers only [28] or simply non-ferromagnetic phase [27]. One successful study combines density functional theory (DFT) with many body dynamical mean-field theory (DFT+DMFT), which can reproduce the metal–insulator transition in SRO thin film and the antiferromagnetic insulator property in SRO monolayer [29]. However, a successful route toward the desired ultrathin spin-polarized (SP) layer hosting the SP-2DEG based on SRO is still lacking.

In this paper, we study the electronic and magnetic properties of SRO through ab initio calculations using the LDA +  $U$  method. Based on the Heisenberg model, we simulate the Curie temperature of bulk SRO by the usual mean-field method, self-consistent Gaussian approximation (SCGA) [30] and Monte Carlo (MC) method [31]. We successfully reproduced the Curie temperature of bulk SRO from the intersite exchange parameters given by DFT +  $U$  calculations. Moreover, we show that, by taking the on-site energy of both Ru and Ti ions into consideration, the metal–insulator transition in single layer SRO associated with the transition from half-metallic ferromagnetism to insulating antiferromagnetism can be induced by tuning the lattice constant from the SRO to STO one. Therefore, the half-metallic phase of single layer SRO in SRO/STO superlattice can be achieved by manipulating the strain effect or applying an external lateral stress. Our work thus paves a new way toward the desired ultrathin SP-2DEG based on SRO.

## 2. Method

First-principles calculations are performed using the Vienna ab initio simulation package (VASP) [32–34] based on the density functional theory (DFT). The projector augmented wave (PAW) [35,36] pseudopotentials with the exchange correlation energy term from Ceperley–Alder [37] and Perdew–Zunger [38] (CA-PZ) type local density approximation (LDA) [39] are used in this work. To account for the strong-correlations in  $d$ -orbitals, we include the on-site Coulomb repulsion  $U$  (LDA +  $U$ ) [40] with  $U = 3.5$  eV,  $J = 0.6$  eV for Ru ions [20]. Different  $U$  and  $J$  values for Ru ions are also considered to see the effects. The reasonable  $U$  value of Ti ions ranges from 3.5 to 8.0 eV [41–44]. Because the lattice constants and the bulk modulus of bulk STO agree better with experimental results [42], we thus adopt the on-site  $U = 5.0$  eV,  $J = 0.64$  eV for Ti ions [41,42]. Owing to the same ionicity of Ru(Ti) ions and the same local  $\text{RuO}_6(\text{TiO}_6)$  octahedral structure, the same  $U$  and  $J$  values of Ru(Ti) ions are adopted for both bulk and monolayer systems. The  $k$ -mesh and energy cutoff are  $12 \times 12 \times 8$  ( $8 \times 8 \times 1$ ) and 400 eV for bulk SRO (SRO/STO superlattice). In all calculations, the lattice structure is optimized until the total energy converges within  $10^{-3}$  eV. The Curie temperature ( $T_C$ ) of the ferromagnetic phase are simulated through the Monte Carlo method based on the Heisenberg model using the VAMPIRE package [31]. A  $50 \times 50 \times 50$  ( $50 \times 50 \times 1$ ) supercell for bulk SRO (SRO/STO superlattice) is used in Monte Carlo simulations.

## 3. Results

### 3.1. Bulk Properties of SRO

Firstly, we discuss the electronic and magnetic properties of bulk SRO in this section. The counterpart for the single layer SRO in SRO/STO superlattice is discussed in the next section. SRO crystallizes in the perovskite structure similar to many transition metal oxides such as  $\text{SrTiO}_3$  and  $\text{LaRuO}_3$ . Each Ru ion is surrounded by six O ions forming an  $\text{RuO}_6$  octahedron. At low temperature, SRO transits from space group  $Pm\bar{3}m$  of the original  $1 \times 1$  perovskite unit cell into  $Pbnm$  (#62,  $D_{2h}^{16}$ ) with a lower symmetry and a larger  $\sqrt{2} \times \sqrt{2} \times 2$  supercell [13] by rotating the  $\text{RuO}_6$  octahedrons, as shown in Figure 1a.

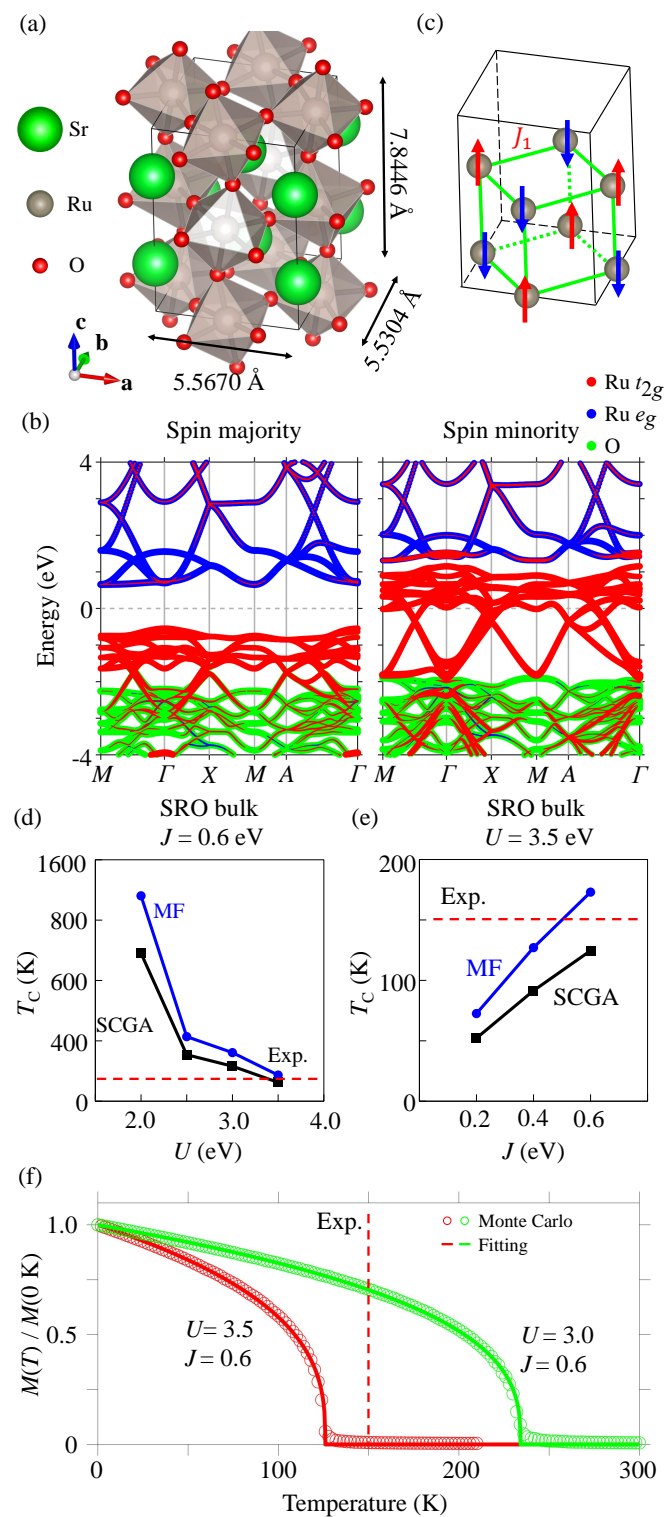


**Figure 1.** (a) The crystal structure of SrRuO<sub>3</sub>. (b) Calculated band structures of SRO from LDA + U. The colors indicate different orbital components. (c) The G-type antiferromagnetism spin configuration of SRO. (d) The mean field and SCGA. (e) Curie temperatures of bulk SRO with different  $U$  and  $J$ . The experimental  $T_c$  is shown in red dashed line. (f) The Monte Carlo simulations of Curie temperatures. The colors indicate different  $U$  and  $J$ . The lines are the fitted curves for the data points given from Monte Carlo simulations. The red dashed line indicate the experiment result.

The LDA +  $U$  band structures of SRO in Figure 1b show the half-metallic behavior, that is, the majority spin channel shows a Mott insulating energy band gap at the Fermi level ( $E_F$ ), while the spin minority channel is metallic. Therefore, only the spin down electrons can conduct, resulting in 100% spin polarization at  $E_F$  which is ideal for spintronics. The orbital projections of the band structure demonstrate that the band gap in the majority spin channel is between the Ru- $t_{2g}(d_{xy}, d_{xz}, d_{yz})$  and  $e_g(d_{x^2-y^2}, d_{z^2})$  bands. These half-metal characters are the same as those in previous experimental observations [17–19] as well as ab initio calculations including LDA +  $U$  [20], DMFT method [21], and GW method [45].

Based on these LDA +  $U$  results, we then simulate the Curie temperature  $T_C$  by considering the Heisenberg model:

$$H = -\frac{1}{2} \sum_{ij} J_i \mathbf{S}_j \cdot \mathbf{S}_i. \quad (1)$$

Here,  $J_i$  is the intersite exchange parameter between different magnetic (Ru) ions and  $\mathbf{S}_i$  indicates the unit vector of the spin direction. These  $J_i$  values can be calculated from the DFT total energies of different magnetic phases. Beside the above ferromagnetic (FM) phase, we have also calculated the DFT total energy of SRO in the G-type antiferromagnetic (AFM) phase, as shown in Figure 1c. The exchange parameter  $J_1$  between nearest-neighbor Ru ions is then calculated by

$$J_1 = (E_{AFM} - E_{FM}) / (N_{nn} \cdot N_{mag}). \quad (2)$$

Here, the  $E_{AFM}(E_{FM})$  is the total energy of the AFM (FM) phase,  $N_{mag}$  is the number of magnetic Ru ions in the unit cell and  $N_{nn}$  is the number of nearest-neighbor Ru ions of each Ru ion. Since the Ru sublattice is of the simple cubic structure, the number  $N_{nn} = 6$ , while  $N_{mag} = 4$  because the SRO  $\sqrt{2} \times \sqrt{2} \times 2$  unit cell is composed of four simple perovskite  $1 \times 1 \times 1$  unit cells. Thus, we obtain  $J_1 \simeq 7.455$  meV.

Several approaches can be used to estimate  $T_C$  based on the Heisenberg model. The simplest one is the mean field (MF) method:

$$T_C^{MF} \simeq \frac{1}{3} N_{nn} J_1. \quad (3)$$

This gives  $T_C^{MF} \simeq 173.0$  K, which is somewhat larger than the experimental  $T_{C,SRO} \simeq 150$  K [13]. As in the usual cases, the mean field method overestimates the  $T_C$  value of SRO. Thus, we also adopt the self-consistent Gaussian approximation (SCGA) method [30].

$$T_C^{SCGA} \simeq \theta_C T_C^{MF}. \quad (4)$$

Here,  $\theta_C$  is a structure dependent parameter. Because the Ru ions are arranged in the simple cubic structure, the parameter  $\theta_C \simeq 0.719$  is used accordingly [30]. The Curie Temperature calculated by the SCGA method is  $T_C^{SCGA} \simeq 124.6$  K, which is 16% underestimated in comparison with the experiment result  $T_{C,SRO} \simeq 150$  K [13].

To see the influence of on-site Coulomb repulsion  $U$  and exchange  $J$  on  $T_C$ , we have done DFT total energy calculations with  $U$  ranging from 2.0 eV to 3.5 eV and  $J$  ranging from 0.2 eV to 0.6 eV. The estimated  $T_C$  values are presented in Figure 1d. As can be seen in the figure, the highly overestimated  $T_C$  with  $U = 2.0$  eV decreases along with increasing  $U$ . With the  $U$  value of 3.5 eV, the estimated  $T_C$  approaches the experimental  $T_C$ . This behavior that the on-site  $U$  can lower the  $T_C$  of SRO is compatible with the Goodenough–Kanamori superexchange rule that the Hubbard  $U$  can stabilize the AFM phase. On the other hand, the on-site exchange  $J$  plays a different role to enhance  $T_C$ , as shown in Figure 1e. It should be noted that, in addition to Hubbard  $U$ ,  $T_C$  is also sensitive to the on-site exchange  $J$  in the opposite direction. These contrary trends imply that the Liechtenstein’s rotationally invariant LDA +  $U$  scheme [40] and the Dudarev’s simplified LDA +  $U$  scheme [46], which takes  $U_{eff} \equiv U - J$  as a single parameter, could lead to different behavior of the Curie temperature.

Furthermore, we also perform the Monte Carlo simulations for the magnetizations of SRO as functions of temperature based on the Heisenberg model with  $U, J = 3.5, 0.6$  eV and  $U, J = 3.0, 0.6$  eV, as presented in Figure 1f. We then fit the Monte Carlo magnetizations by the formula  $M(T) = M(0\text{ K}) (1 - T/T_C^{\text{MC}})^{\beta}$  to estimate  $T_C^{\text{MC}}$  with the fitted curves also depicted in Figure 1f. Here,  $\beta = 0.3456(0.3430)$  is the critical exponent for the  $U = 3.5(3.0)$  eV case. Surprisingly, for both cases with different  $U$  values of 3.0 and 3.5 eV, our Monte Carlo  $T_C$  values agree well with our SCGA  $T_C$  within 2%. Moreover, for  $U, J = 3.5, 0.6$  eV, the estimated  $T_C^{\text{MC}} \simeq 126$  K is close to the experimental  $T_C \simeq 150$  K. Consequently our LDA +  $U$  calculations and Monte Carlo  $T_C$  simulations for SRO are reliable.

### 3.2. Monolayer SRO in SRO/STO Superlattice

To study the phase transition of the single layer (1 u.c.) SRO, we consider the SRO/STO superlattice containing 1 u.c. SRO and 5 u.c. STO in the (001) direction. The distorted  $\text{TiO}_6$  oxide octahedron in bulk STO, which rotates in the antiferrodistortive structure [47], is used as the initial structure, as shown in Figure 2a,b. To take the strong correlation into account, we apply on-site  $U = 3.5$  eV and  $J = 0.6$  eV for Ru-4d orbital and  $U = 5.0$  eV and  $J = 0.64$  eV for Ti-3d orbital. To study the lateral strain induced metal-insulator transition, we tune the lattice constants  $a, b$  of the SRO/STO superlattice from the SRO  $\sqrt{2} \times \sqrt{2} \times 2$  lattice parameters  $a = 5.5670, b = 5.5304$  (denoted as  $\lambda = 0$ ) to the STO lattice parameters  $a = b = 5.5225$  (or  $a/\sqrt{2} = 3.905$  in  $1 \times 1$  u.c.) (denoted as  $\lambda = 1$ ) with the parameter  $\lambda$  indicating the strain effect. We then optimize the  $c$ -axis as well as the ion positions with lattice  $a, b$  fixed at a given  $\lambda$ . Three different magnetic phases, including paramagnetic, ferromagnetic (FM) and antiferromagnetic (AFM), of the SRO layer are considered as discussed below.

The electronic structures of three different magnetic phase of  $(\text{SRO})^1/(\text{STO})^5$  superlattice are shown in Figure 2c–h. For the paramagnetic phase (Figure 2c,d), the band structures of spin up and spin down channels degenerate owing to the time reversal symmetry and spin rotational symmetry. The orbitals near the Fermi level are dominated by Ru  $d$  orbitals. The Ru  $t_{2g}$  and Ru  $e_g$  bands cross each other showing metallic behaviors. The orbital decomposition also presents a spin-unpolarized two-dimensional electron gas (2DEG) conducted by Ru  $t_{2g}$  orbitals. On the other hand, for the ferromagnetic phase shown in Figure 2e,f, the spin up Ru  $e_g$  and  $t_{2g}$  bands split with each other and hence open an energy gap of 0.52 eV at the Fermi level ( $E_F$ ), whereas the spin down channel remains gapless. Therefore, the ferromagnetic phase shows the half-metallic character, in which one spin channel is conducting while the other is insulating, similar to the fully spin polarized metallic behavior in bulk SRO. More importantly, this half-metallic single u.c. SRO in  $(\text{SRO})^1/(\text{STO})^5$  superlattice demonstrates the desired ultrathin fully spin-polarized (SP) 2DEG within a single layer, same as previous studies. As for the antiferromagnetic phase shown in Figure 2g,h, there exists a small energy gap  $\sim 0.12$  eV between  $e_g$  and  $t_{2g}$  bands, leading to the antiferromagnetic insulator. Total energy analysis shows that the half-metallic FM phase is energetically most favorable and is thus the ground state among all the three phase, while the paramagnetic phase is of the highest total energy. However, the total energy of the AFM phase is only 0.47 meV higher than that of the FM phase, indicating that the insulating AFM phase could also be observed experimentally. Previous studies also show that the doping or interdiffusion of Ti ions may enhance the insulating phase [48–50] in real systems.

To study the strain effect originated from the lattice mismatch between SRO and STO in the SRO/STO superlattice, we tune the lattice parameters  $a$  and  $b$  with the order parameter  $\lambda = 0$  representing the bulk SRO lattice parameters  $a$  and  $b$ , and  $\lambda = 1$  corresponding to the bulk STO lattice parameters  $a, b$ . The  $c$ -axis and ion positions are optimized for all cases. Similar to the previous section, we perform electronic structure calculations and Monte Carlo simulations for AFM and FM phases. To determine the intersite exchange parameters, we use  $N_{\text{nn}} = 4$  for the nearest-neighbor Ru ions and  $N_{\text{mag}} = 2$  for the two magnetic ions in the superlattice in Equation (2). Figure 3a shows the calculated  $T_C^{\text{MF}}$  with different lattice constants (strains). For  $U^{\text{Ru}} = 3.5$  eV and  $U^{\text{Ti}} = 5.0$  eV (square), the  $T_C^{\text{MF}}$  decreases with increasing  $\lambda$ , similar to previous conclusions of the lattice effect on the SRO magnetic

phase (cf. [51,52]). Precisely for  $\lambda = 0$ , the  $J_1 \simeq 2.53$  meV and  $T_C^{MF} \simeq 39.2$  K. However, with  $\lambda = 1$ , as described in the previous paragraph, the energy difference between FM and AFM phases becomes fairly small and the  $T_C^{MF}$  is only 0.5 K with  $J_1 \simeq 0.059$  meV.

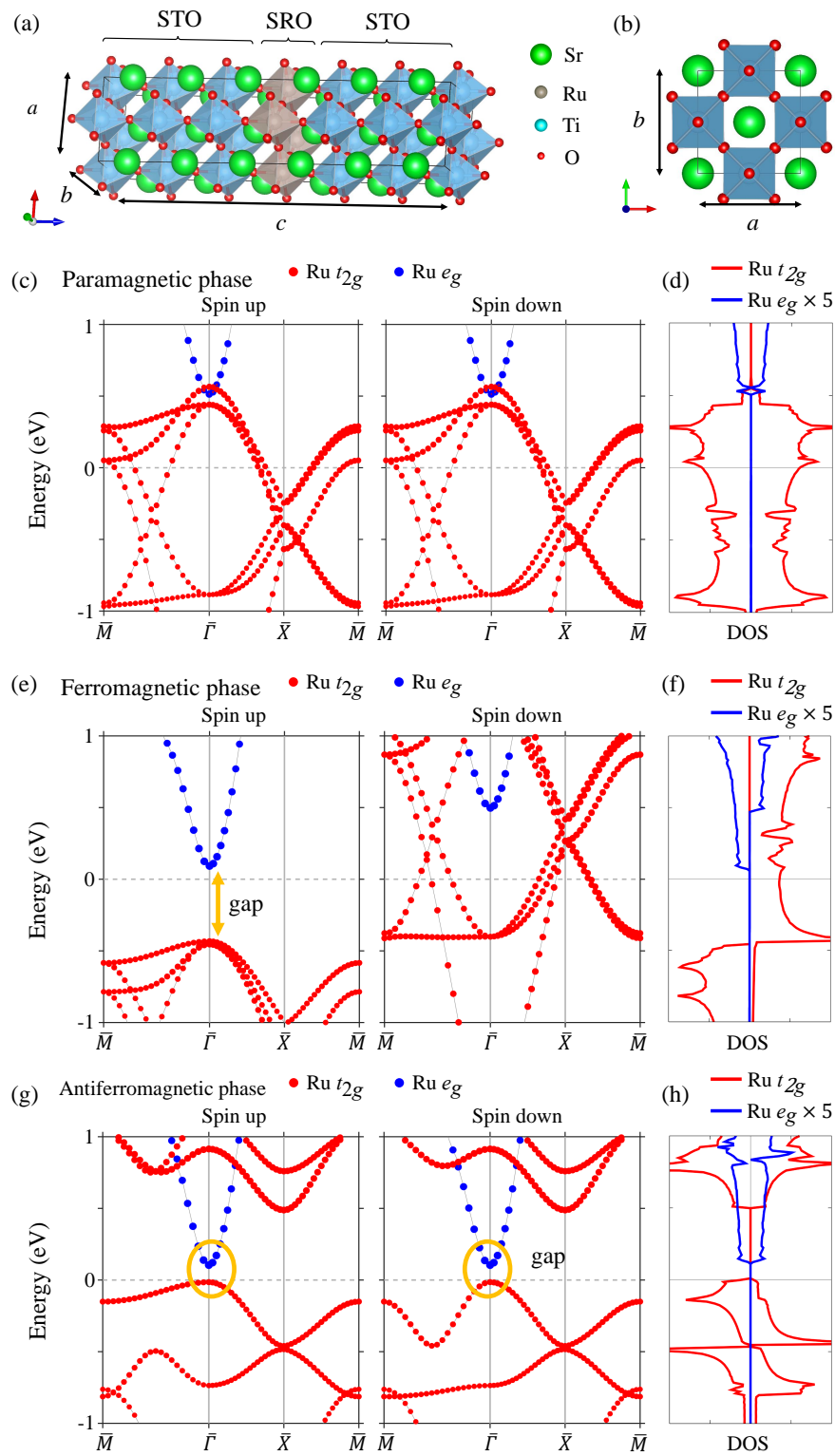


**Figure 2.** Side (a) and top (b) view of the  $(\text{SRO})^1/(\text{STO})^5$  superlattice structure used in the calculations. (c,e,g) Band structures of three magnetic phases of  $(\text{SRO})^1/(\text{STO})^5$  superlattice. The red (blue) dots present the component of Ru  $t_{2g}$  and  $e_g$  orbitals. The orange circle and arrow highlight the band gap. (d,f,h) The total density of states of each magnetic phase.

The strong correlations in Ti *d* orbitals also play an important role in this system. As also shown in Figure 3a, by tuning the order parameter  $\lambda$  with  $U^{\text{Ti}} = 0$  (circle), the energy difference between FM and AFM phases becomes larger and hence makes the  $T_C^{\text{MF}}$  much higher, strongly stabilizing the FM half-metallic phase. The  $T_C^{\text{MF}} \approx 78$  K for  $\lambda = 0$  decreases to 59.7 K with  $\lambda = 1$ . In other words, the strong correlations in Ti ions help stabilize the AFM insulating phase and thus achieve the FM–AFM metal–insulator phase transition upon lateral strain.

The Monte Carlo calculations of Curie temperature are also accomplished for the (SRO)<sup>1</sup>/(STO)<sup>5</sup> superlattice, as presented in Figure 3c,d. Different from the zero magnetism at high temperature for the bulk systems (Figure 1f), the magnetism does not vanish at high temperatures for the superlattice cases. This is due to the Heisenberg model and the Mermin–Wagner theorem for two dimensional systems which conclude that there is no phase transition in a two-dimensional system. To simulate the Curie temperature, the magnetism of Monte Carlo results with  $M(T) > 0.2$  are fitted by  $M(T) = M(0\text{ K}) (1 - T/T_C^{\text{MC}})^p$  with the critical exponents ranging from 0.42 to 0.50 (Figure 3c,d). As shown Figure 3a, the MC and MF results both show the same trend with more or less a constant ratio  $T_C^{\text{MC}}/T_C^{\text{MF}}$  by tuning  $\lambda$  and  $U^{\text{Ti}}$ . The only difference is that the MF method always overestimates the Curie temperature for all the considered systems.

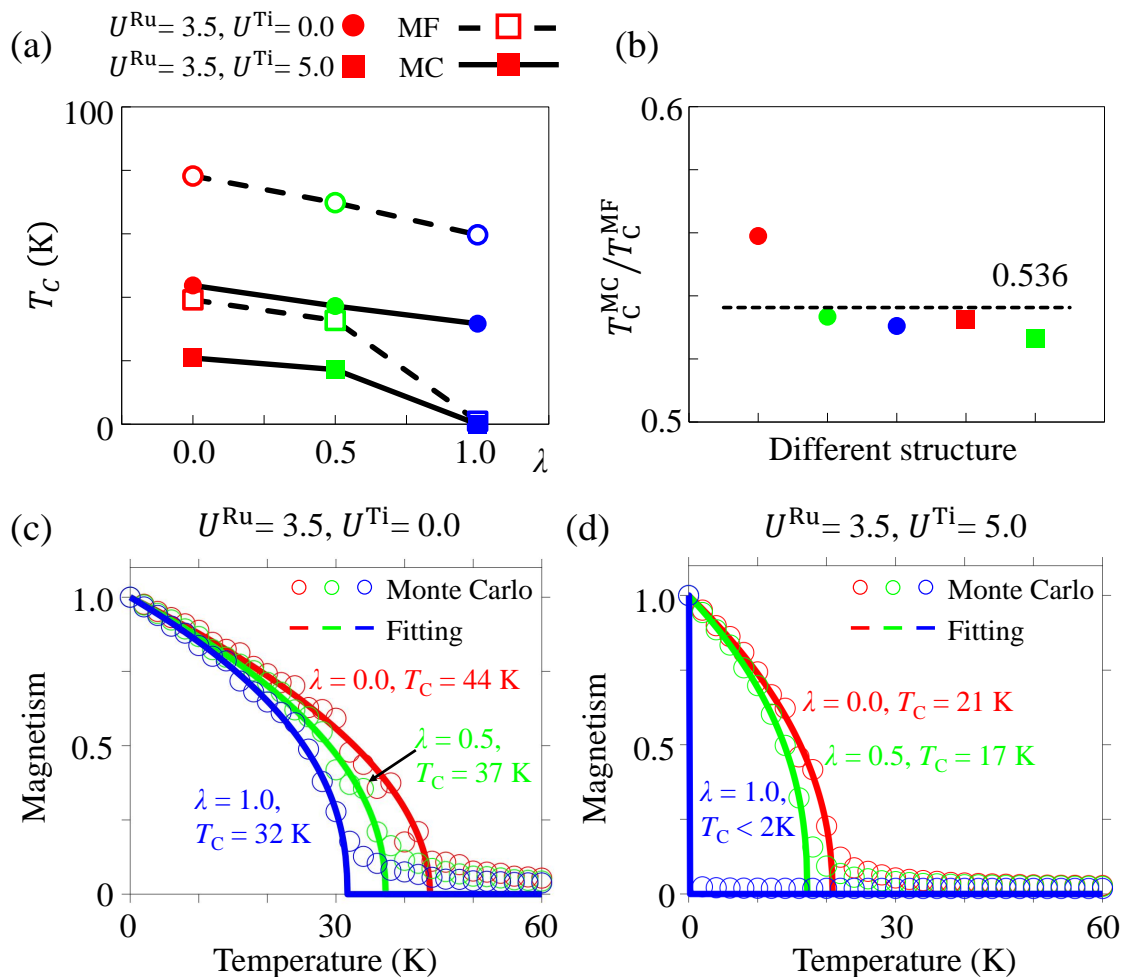


**Figure 3.** (a) Mean field and Monte Carlo  $T_C$  of different lattice constants and  $U^{\text{Ti}}$  in SRO/STO superlattice.  $\lambda = 0$  indicates using the SRO lattice constants  $a, b$ , while  $\lambda = 1$  indicates that the STO lattice constants  $a, b$  are used. The solid (dashed) line indicates the Monte Carlo (mean field) result. The circle (square) symbol indicates the  $U^{\text{Ti}} = 0$  eV (5.0 eV) cases. (b) The ratio  $T_C^{\text{MC}}/T_C^{\text{MF}}$  of all considered cases. The dashed line represents the average ratio of 0.536. (c,d) The Monte Carlo and the fitting magnetization of SRO/STO superlattice.

#### 4. Discussion

Previous DFT studies on SrRuO<sub>3</sub> show different magnetic phases in 1 u.c. SRO including ferromagnetic and paramagnetic ones. Many-body simulations by dynamical mean-field theory (DMFT) show AFM insulator of 1 u.c. SRO in SRO/STO superlattice. Thus far, no insulating phases of 1 u.c. thickness SRO are reported by DFT calculations. Our study demonstrates that the antiferromagnetic insulating phase in 1 u.c. SRO can be obtained in the single particle picture. In addition, the lattice constant and on-site energy of Ti play an important role in this magnetic metal–insulator transition. More importantly, our results agree well with the experimental findings in which tensile strain can affect the Curie temperature in SRO thin film [51,52].

Note that the MIT of the SRO monolayer could have several sources such as the defect effect, inter-diffusion, layer thickness, as well as the strain effect and magnetic phase transition as studied in this work. Particularly, the SRO/STO interface exhibits intermixing on a length scale of 1~1.5 unit cells [53]. Thus, the impurities and intermixing may also play an important role in MIT of SRO monolayer. However, among the aforementioned several effects that could cause MIT of SRO monolayer, we focus on the strain induced magnetic phase transition associated MIT of SRO monolayer. Our study offers a route to tuning the electric and magnetic properties of SRO monolayer, and could be generalized to SRO multilayers.

Our aforementioned conclusions are slightly different from those from previous study using DFT + DMFT [29]. In a previous DMFT study, Si et al. [29] claimed SRO thin films are always antiferromagnetic insulator even under the lattice stress of  $\pm 0.5\%$ . Differences in computational methods between our work and previous studies are discussed below. Firstly, we use the experimental STO lattice constant of 5.5225 while the previous study [29] uses the optimized lattice constant of  $3.95 \times \sqrt{2} = 5.5861$ , differing from the former by 1.2%. Secondly, the lattice structure is optimized using the PBE+mBJ method in the previous study [29], even though mBJ method actually does not contribute to atomic forces. We use LDA +  $U$  method to optimize our atomic positions. Thirdly, all calculations in the previous studies do not consider the on-site Hubbard energy of Ti  $d$  orbitals.

To realize the room temperature ultra-thin spin-polarized two-dimensional electron gas is an important issue [25,29]. From our calculations, the intersite exchange field  $J_1$  can be modified by lateral strain through tuning the lattice parameter  $a$  and  $b$ . Therefore, the FM half-metallic phase in monolayer SRO can be induced by applying the external tensile lateral strain. Experimentally, this can be achieved by growing SRO on another perovskite with similar lattice constants as SRO, i.e., larger lattice parameters than the STO ones. This pave a new route toward realizing the desirable ultra-thin spin-polarized 2DEG for future spintronics.

Owing to the inability of handling two-dimensional systems by the self-consistent Gaussian approximation (SCGA), the  $T_C^{\text{SCGA}}$  of the SRO layer in (SRO)<sup>1</sup>/(STO)<sup>5</sup> superlattice cannot be calculated. However, combining our MC and MF results, we can estimate the SCGA counterparts by  $\theta_C = T_C^{\text{MC}}/T_C^{\text{MF}}$ . As shown in Figure 3b and discussed previously,  $\theta_C \simeq 0.536$ . This parameter also gives a convenient method to estimate the two-dimensional square lattice such as the other two-dimensional magnetic perovskite.

#### 5. Conclusions

In this paper, we perform first-principles electronic calculations as well as Monte Carlo  $T_C$  simulations for single layer SRO in SRO/STO superlattice. We discover a metal–insulator transition associated with FM–AFM transition of SRO single layer in SRO/STO superlattice. This combined transition is sensitive to the lattice mismatch, strong correlation, as well as the interlayer electronic interactions. We demonstrate that the bulk ferromagnetic metallicity can be restored in single layer SRO in SRO/STO superlattice by manipulating the strain effect, giving rise to spin polarized half-metallic 2D SRO layer beyond the experimental observation of AFM insulating thin films. Moreover, based on the Heisenberg model, the accurate Curie temperate is estimated by three different methods including the mean field, SCGA, and Monte Carlo simulations. The mean field method, as in usual cases,

overestimates the  $T_C$  in both bulk and thin film SRO. While the SCGA and Monte Carlo methods yield excellent  $T_C$  consistent with the experimental  $T_C$  for the bulk phase. For the single layer SRO in the SRO/STO superlattice, we predict the Curie temperature of the SRO layer ranging from  $\sim 20$  to  $\sim 40$  K. Furthermore, this  $T_C$  can be increased by applying an external lateral stress. Our results present a new route to implement the ultrathin spin-polarized 2DEG.

**Author Contributions:** A.H. performed band structures calculations and prepared the original draft. S.-H.H. performed Curie temperature simulations and prepared the original draft. H.-T.J. supervised the project and reviewed and edited the manuscript.

**Funding:** This research received no external funding.

**Acknowledgments:** This work was supported by the Ministry of Science and Technology, Taiwan. H.-T.J. also thanks NCHC and CINC-NTU, Taiwan for technical support.

**Conflicts of Interest:** The authors declare no conflict of interest.

## References

1. Ikeda, S.; Miura, K.; Yamamoto, H.; Mizunuma, K.; Gan, H.D.; Endo, M.; Kanai, S.; Hayakawa, J.; Matsukura, F.; Ohno, H. A perpendicular-anisotropy CoFeB-MgO magnetic tunnel junction. *Nat. Mater.* **2010**, *9*, 721–724. [[CrossRef](#)] [[PubMed](#)]
2. Kubota, H.; Fukushima, A.; Yakushiji, K.; Nagahama, T.; Yuasa, S.; Ando, K.; Maehara, H.; Nagamine, Y.; Tsunekawa, K.; Djayaprawira, D.D.; et al. Quantitative measurement of voltage dependence of spin-transfer torque in MgO-based magnetic tunnel junctions. *Nat. Phys.* **2007**, *4*, 37–41. [[CrossRef](#)]
3. Wang, W.G.; Li, M.; Hageman, S.; Chien, C.L. Electric-field-assisted switching in magnetic tunnel junctions. *Nat. Mater.* **2011**, *11*, 64–68. [[CrossRef](#)] [[PubMed](#)]
4. Fang, D.; Kurebayashi, H.; Wunderlich, J.; Vyborny, K.; Zarbo, L.P.; Campion, R.P.; Casiraghi, A.; Gallagher, B.L.; Jungwirth, T.; Ferguson, A.J. Spin-orbit-driven ferromagnetic resonance. *Nat. Nanotechnol.* **2011**, *6*, 413–417. [[CrossRef](#)] [[PubMed](#)]
5. Sankey, J.C.; Cui, Y.-T.; Buhrman, R.A.; Ralph, D.C.; Sun, J.Z.; Slonczewski, J.C. Measurement of the spin-transfer-torque vector in magnetic tunnel junctions. *Nat. Phys.* **2007**, *4*, 67–71. [[CrossRef](#)]
6. Slonczewski, J.C. Conductance and exchange coupling of two ferromagnets separated by a tunneling barrier. *Phys. Rev. B* **1989**, *39*, 6995–7002. [[CrossRef](#)]
7. Reyren, N.; Thiel, S.; Caviglia, A.D.; Kourkoutis, L.F.; Hammerl, G.; Richter, C.; Schneider, C.W.; Kopp, T.; Rüetschi, A.S.; Jaccard, D.; et al. Superconducting Interfaces Between Insulating Oxides. *Science* **2007**, *317*, 1196–1199. [[CrossRef](#)] [[PubMed](#)]
8. Ohtomo, A.; Hwang, H.Y. A high-mobility electron gas at the LaAlO<sub>3</sub>/SrTiO<sub>3</sub> heterointerface. *Nature* **2004**, *427*, 423–426. [[CrossRef](#)] [[PubMed](#)]
9. Burton, J.D.; Tsymbal, E.Y. Prediction of electrically induced magnetic reconstruction at the manganite/ferroelectric interface. *Phys. Rev. B* **2009**, *80*, 174406. [[CrossRef](#)]
10. Chen, H.; Qiao, Q.; Marshall, M.S.J.; Georgescu, A.B.; Gulec, A.; Phillips, P.J.; Klie, R.F.; Walker, F.J.; Ahn, C.H.; Ismail-Beigi, S. Reversible Modulation of Orbital Occupations via an Interface-Induced Polar State in Metallic Manganites. *Nano Lett.* **2014**, *14*, 4965–4970. [[CrossRef](#)] [[PubMed](#)]
11. Lu, H.; George, T.A.; Wang, Y.; Ketsman, I.; Burton, J.D.; Bark, C.-W.; Ryu, S.; Kim, D.J.; Wang, J.; Binek, C.; et al. Electric modulation of magnetization at the BaTiO<sub>3</sub>/La<sub>0.67</sub>Sr<sub>0.33</sub>MnO<sub>3</sub> interfaces. *Appl. Phys. Lett.* **2012**, *100*, 232904. [[CrossRef](#)]
12. Yu, P.; Lee, J.S.; Okamoto, S.; Rossell, M.D.; Huijben, M.; Yang, C.H.; He, Q.; Zhang, J.X.; Yang, S.Y.; Lee, M.J.; et al. Interface Ferromagnetism and Orbital Reconstruction in BiFeO<sub>3</sub>–La<sub>0.7</sub>Sr<sub>0.3</sub>MnO<sub>3</sub> Heterostructures. *Phys. Rev. Lett.* **2010**, *105*, 027201. [[CrossRef](#)] [[PubMed](#)]
13. Koster, G.; Klein, L.; Siemons, W.; Rijnders, G.; Dodge, J.S.; Eom, C.B.; Blank, D.H.A.; Beasley, M.R. Structure, physical properties, and applications of SrRuO<sub>3</sub> thin films. *Rev. Mod. Phys.* **2012**, *84*, 253–298. [[CrossRef](#)]
14. Das, S.; Herklotz, A.; Pippel, E.; Guo, E.J.; Rata, D.; Dörr, K. Strain dependence of antiferromagnetic interface coupling in La<sub>0.7</sub>Sr<sub>0.3</sub>MnO<sub>3</sub>/SrRuO<sub>3</sub> superlattices. *Phys. Rev. B* **2015**, *91*, 134405. [[CrossRef](#)]

15. Ke, X.; Belenky, L.J.; Lauter, V.; Ambaye, H.; Bark, C.W.; Eom, C.B.; Rzechowski, M.S. Spin Structure in an Interfacially Coupled Epitaxial Ferromagnetic Oxide Heterostructure. *Phys. Rev. Lett.* **2013**, *110*, 237201. [[CrossRef](#)] [[PubMed](#)]
16. Ziese, M.; Bern, F.; Pippel, E.; Hesse, D.; Vrejoiu, I. Stabilization of Ferromagnetic Order in  $\text{La}_{0.7}\text{Sr}_{0.3}\text{MnO}_3/\text{SrRuO}_3$  Superlattices. *Nano Lett.* **2012**, *12*, 4276–4281. [[CrossRef](#)] [[PubMed](#)]
17. Nadgorny, B.; Osofsky, M.S.; Singh, D.J.; Woods, G.T.; Soulen, R.J.; Lee, M.K.; Bu, S.D.; Eom, C.B. Measurements of spin polarization of epitaxial  $\text{SrRuO}_3$  thin films. *Appl. Phys. Lett.* **2003**, *82*, 427–429. [[CrossRef](#)]
18. Raychaudhuri, P.; Mackenzie, A.P.; Reiner, J.W.; Beasley, M.R. Transport spin polarization in  $\text{SrRuO}_3$  measured through point-contact Andreev reflection. *Phys. Rev. B* **2003**, *67*, 020411. [[CrossRef](#)]
19. Sanders, J.; Woods, G.T.; Poddar, P.; Srikanth, H.; Dabrowski, B.; Kolesnik, S. Spin polarization measurements on polycrystalline strontium ruthenates using point-contact Andreev reflection. *J. Appl. Phys.* **2005**, *97*, 10C912. [[CrossRef](#)]
20. Jeng, H.T.; Lin, S.H.; Hsue, C.S. Orbital Ordering and Jahn-Teller Distortion in Perovskite Ruthenate  $\text{SrRuO}_3$ . *Phys. Rev. Lett.* **2006**, *97*, 067002. [[CrossRef](#)] [[PubMed](#)]
21. Kim, M.; Min, B.I. Nature of itinerant ferromagnetism of  $\text{SrRuO}_3$ : A DFT+DMFT study. *Phys. Rev. B* **2015**, *91*, 205116. [[CrossRef](#)]
22. Jeong, D.W.; Choi, H.C.; Kim, C.H.; Chang, S.H.; Sohn, C.H.; Park, H.J.; Kang, T.D.; Cho, D.Y.; Baek, S.H.; Eom, C.B.; et al. Temperature Evolution of Itinerant Ferromagnetism in  $\text{SrRuO}_3$  Probed by Optical Spectroscopy. *Phys. Rev. Lett.* **2013**, *110*, 247202. [[CrossRef](#)] [[PubMed](#)]
23. Kostic, P.; Okada, Y.; Collins, N.C.; Schlesinger, Z.; Reiner, J.W.; Klein, L.; Kapitulnik, A.; Geballe, T.H.; Beasley, M.R. Non-Fermi-Liquid Behavior of  $\text{SrRuO}_3$ : Evidence from Infrared Conductivity. *Phys. Rev. Lett.* **1998**, *81*, 2498–2501. [[CrossRef](#)]
24. Laad, M.S.; Müller-Hartmann, E. Origin of the Non-Fermi Liquid Behavior of  $\text{SrRuO}_3$ . *Phys. Rev. Lett.* **2001**, *87*, 246402. [[CrossRef](#)] [[PubMed](#)]
25. Verissimo-Alves, M.; García-Fernández, P.; Bilc, D.I.; Ghosez, P.; Junquera, J. Highly Confined Spin-Polarized Two-Dimensional Electron Gas in  $\text{SrTiO}_3/\text{SrRuO}_3$  Superlattices. *Phys. Rev. Lett.* **2012**, *108*, 107003. [[CrossRef](#)] [[PubMed](#)]
26. Shen, X.; Qiu, X.; Su, D.; Zhou, S.; Li, A.; Wu, D. Thickness-dependent metal–insulator transition in epitaxial  $\text{SrRuO}_3$  ultrathin films. *J. Appl. Phys.* **2015**, *117*, 015307. [[CrossRef](#)]
27. Chang, Y.J.; Kim, C.H.; Phark, S.H.; Kim, Y.S.; Yu, J.; Noh, T.W. Fundamental Thickness Limit of Itinerant Ferromagnetic  $\text{SrRuO}_3$  Thin Films. *Phys. Rev. Lett.* **2009**, *103*, 057201. [[CrossRef](#)] [[PubMed](#)]
28. Gupta, K.; Mandal, B.; Mahadevan, P. Strain-induced metal–insulator transition in ultrathin films of  $\text{SrRuO}_3$ . *Phys. Rev. B* **2014**, *90*, 125109. [[CrossRef](#)]
29. Si, L.; Zhong, Z.; Tomczak, J.M.; Held, K. Route to room-temperature ferromagnetic ultrathin  $\text{SrRuO}_3$  films. *Phys. Rev. B* **2015**, *92*, 041108. [[CrossRef](#)]
30. Garanin, D.A. Self-consistent Gaussian approximation for classical spin systems: Thermodynamics. *Phys. Rev. B* **1996**, *53*, 11593–11605. [[CrossRef](#)]
31. Evans, R.F.L.; Fan, W.J.; Chureemart, P.; Ostler, T.A.; Ellis, M.O.A.; Chantrell, R.W. Atomistic spin model simulations of magnetic nanomaterials. *J. Phys. Condens. Matter* **2014**, *26*, 103202. [[CrossRef](#)] [[PubMed](#)]
32. Kresse, G.; Hafner, J. Ab initio molecular dynamics for open-shell transition metals. *Phys. Rev. B* **1993**, *48*, 13115. [[CrossRef](#)]
33. Kresse, G.; Furthmüller, J. Efficiency of ab-initio total energy calculations for metals and semiconductors using a plane-wave basis set. *Comput. Mater. Sci.* **1996**, *6*, 15–50. [[CrossRef](#)]
34. Kresse, G.; Furthmüller, J. Efficient iterative schemes for ab initio total-energy calculations using a plane-wave basis set. *Phys. Rev. B* **1996**, *54*, 11169. [[CrossRef](#)]
35. Blöchl, P.E. Projector augmented-wave method. *Phys. Rev. B* **1994**, *50*, 17953. [[CrossRef](#)]
36. Kresse, G.; Joubert, D. From ultrasoft pseudopotentials to the projector augmented-wave method. *Phys. Rev. B* **1999**, *59*, 1758. [[CrossRef](#)]
37. Ceperley, D.M.; Alder, B.J. Ground State of the Electron Gas by a Stochastic Method. *Phys. Rev. Lett.* **1980**, *45*, 566. [[CrossRef](#)]
38. Perdew, J.P.; Zunger, A. Self-interaction correction to density-functional approximations for many-electron systems. *Phys. Rev. B* **1981**, *23*, 5048–5079. [[CrossRef](#)]

39. Kohn, W.; Sham, L.J. Self-Consistent Equations Including Exchange and Correlation Effects. *Phys. Rev.* **1965**, *140*, A1133. [[CrossRef](#)]
40. Liechtenstein, A.I.; Anisimov, V.I.; Zaanen, J. Density-functional theory and strong interactions: Orbital ordering in Mott-Hubbard insulators. *Phys. Rev. B* **1995**, *52*, R5467. [[CrossRef](#)]
41. Pavarini, E.; Biermann, S.; Poteryaev, A.; Lichtenstein, A.I.; Georges, A.; Andersen, O.K. Mott Transition and Suppression of Orbital Fluctuations in Orthorhombic  $3d^1$  Perovskites. *Phys. Rev. Lett.* **2004**, *92*, 176403. [[CrossRef](#)] [[PubMed](#)]
42. Kinaci, A.; Sevik, C.; Çağın, T. Electronic transport properties of SrTiO<sub>3</sub> and its alloys: Sr<sub>1-x</sub>La<sub>x</sub>TiO<sub>3</sub> and SrTi<sub>1-x</sub>M<sub>x</sub>O<sub>3</sub> (M = Nb, Ta). *Phys. Rev. B* **2010**, *82*, 155114. [[CrossRef](#)]
43. Solovyev, I.; Hamada, N.; Terakura, K.  $t_{2g}$  versus all 3d localization in LaMO<sub>3</sub> perovskites (M=Ti–Cu): First-principles study. *Phys. Rev. B* **1996**, *53*, 7158–7170. [[CrossRef](#)]
44. Pentcheva, R.; Pickett, W.E. Ionic relaxation contribution to the electronic reconstruction at the *n*-type LaAlO<sub>3</sub>/SrTiO<sub>3</sub> interface. *Phys. Rev. B* **2008**, *78*, 205106. doi:10.1103/PhysRevB.78.205106. [[CrossRef](#)]
45. Ryee, S.; Jang, S.W.; Kino, H.; Kotani, T.; Han, M.J. Quasiparticle self-consistent GW calculation of Sr<sub>2</sub>RuO<sub>4</sub> and SrRuO<sub>3</sub>. *Phys. Rev. B* **2016**, *93*, 075125. [[CrossRef](#)]
46. Dudarev, S.L.; Botton, G.A.; Savrasov, S.Y.; Humphreys, C.J.; Sutton, A.P. Electron-energy-loss spectra and the structural stability of nickel oxide: An LSDA+U study. *Phys. Rev. B* **1998**, *57*, 1505–1509. [[CrossRef](#)]
47. El-Mellouhi, F.; Brothers, E.N.; Lucero, M.J.; Bulik, I.W.; Scuseria, G.E. Structural phase transitions of the metal oxide perovskites SrTiO<sub>3</sub>, LaAlO<sub>3</sub>, and LaTiO<sub>3</sub> studied with a screened hybrid functional. *Phys. Rev. B* **2013**, *87*, 035107. [[CrossRef](#)]
48. Kim, J.; Kim, J.Y.; Park, B.G.; Oh, S.J. Photoemission and x-ray absorption study of the electronic structure of SrRu<sub>1-x</sub>Ti<sub>x</sub>O<sub>3</sub>. *Phys. Rev. B* **2006**, *73*, 235109. [[CrossRef](#)]
49. Kim, K.W.; Lee, J.S.; Noh, T.W.; Lee, S.R.; Char, K. Metal–insulator transition in a disordered and correlated SrTi<sub>1-x</sub>Ru<sub>x</sub>O<sub>3</sub> system: Changes in transport properties, optical spectra, and electronic structure. *Phys. Rev. B* **2005**, *71*, 125104. [[CrossRef](#)]
50. Lin, P.A.; Jeng, H.T.; Hsue, C.S. Electronic structure and orbital ordering of SrRu<sub>1-x</sub>Ti<sub>x</sub>O<sub>3</sub>: GGA + *U* investigations. *Phys. Rev. B* **2008**, *77*, 085118. [[CrossRef](#)]
51. Herklotz, A.; Kataja, M.; Nenkov, K.; Biegalski, M.D.; Christen, H.M.; Deneke, C.; Schultz, L.; Dörr, K. Magnetism of the tensile-strain-induced tetragonal state of SrRuO<sub>3</sub> films. *Phys. Rev. B* **2013**, *88*, 144412. [[CrossRef](#)]
52. Wang, X.W.; Wang, X.; Zhang, Y.Q.; Zhu, Y.L.; Wang, Z.J.; Zhang, Z.D. Magnetic anisotropy and metal–insulator transition in SrRuO<sub>3</sub> thin films at different growth temperatures. *J. Appl. Phys.* **2010**, *107*, 113925. [[CrossRef](#)]
53. Bern, F.; Ziese, M.; Setzer, A.; Pippel, E.; Hesse, D.; Vrejoiu, I. Structural, magnetic and electrical properties of SrRuO<sub>3</sub> films and SrRuO<sub>3</sub>/SrTiO<sub>3</sub> superlattices. *J. Phys. Condens. Matter* **2013**, *25*, 496003. [[CrossRef](#)] [[PubMed](#)]

